Feature Article

Novel framework g-C$_3$N$_4$ film as efficient photoanode for photoelectrochemical water splitting

Xue Lu, Zhifeng Liu[*], Junwei Li, Jing Zhang, Zhengang Guo

School of Materials Science and Engineering, Tianjin Chengjian University, 300384, Tianjin, China

ARTICLE INFO

ABSTRACT

We firstly report the fabrication of the g-C$_3$N$_4$ film with novel framework structure by thermal vapor liquid-polymerization method which grows directly on FTO glass substrate as photoanode for photoelectrochemical (PEC) water splitting to produce hydrogen. The specific growth process for the framework structure of the g-C$_3$N$_4$ film has been discussed in detail. The outstanding PEC performance with an improved photocurrent density of the framework g-C$_3$N$_4$ film is accessed by 89 µA/cm^2 at 1.1 V (vs. RHE), which is higher than that of the g-C$_3$N$_4$ film prepared from g-C$_3$N$_4$ powder. The remarkable PEC performance benefits from the considerable factors as following: (i) the uniformity of film grown on FTO substrate; (ii) the excellent light harvesting ability; (iii) the better optical performance; (iv) the reduced photogenerated electron-hole pairs recombination rate. In addition, this method is extremely facile to prepare g-C$_3$N$_4$ film for water splitting into H$_2$.

1. Introduction

Hydrogen energy, as an alternative green energy source, can be considered as a perfect solution to deal with energy crisis owing to the gradual depletion of fossil fuels. However, over 90% of the hydrogen is produced from steam reforming of methane while it is a non-renewable source [1]. Since the first discovery of photoelectrochemical (PEC) water splitting into hydrogen via using titanium dioxide (TiO$_2$) photoelectrode by Fujishima and Honda [2]. Photocatalytic materials display the great potentiality of solving both environment and energy questions through converting inexhaustible solar energy into clean and environmentally friendly hydrogen. Thus, developing stable and effective photocatalytic materials for the water splitting into H$_2$ has been a research hotspot in material science fields [3]. In practical application, a variety of photocatalytic materials have been utilized, such as metal and nonmetal compound oxides [4,5], sulfides and nitrides [6,7] and so forth. Among them, visible-light photocatalytic materials have drawn widespread attention due to their efficient solar-energy utilization as well as energy production [8].

In particular, metal-free carbon nitride has triggered broad interest owing to its better performances including excellent optical properties, nontoxicity, low cost and facile manufacture,

etc[9,10]. In addition, among its several allotrope phases, the graphite-like carbon nitiride (g-C$_3$N$_4$) has been regarded as the most stable under chemical and thermal conditions [11,12]. So as a visible-light photocatalyst, g-C$_3$N$_4$ has been widely applied for removing pollutants in air and water because of not only its suitable band gap of 2.7 eV but also its charming two-dimensional crystal structure [13,14]. As earlier reported, Dong et al. have prepared g-C$_3$N$_4$ particles via pyrolysing urea, and its ppb-level NO removal ratio is 42% after 30 min, which shows better purification capability in air [15]. Zhang et al. have heated melamine to 550 °C to product bulk g-C$_3$N$_4$, and RhB is degraded ∼26% within 60 min, which indicates the certain photocatalytic activities [16].

Up until now, under high temperature g-C$_3$N$_4$ can be easily polymerized via inexpensive raw materials including urea, melamine, dicyandiamide and so on [17–20]. However most acquired productions by above materials are agglomerate or powder, which is not able to be used repeatedly simply for the degradation of pollutants in water. Apart from that, the bulk or powder g-C$_3$N$_4$ is difficult to applied as a photoelectrode for PEC water splitting into hydrogen, although it possesses a better ability of catalysis under visible light. Obviously, a direct, uniform and continuous g-C$_3$N$_4$ film is a priority not only for the degradation of pollutants in water but also for PEC water splitting into hydrogen [21]. Consequently, some methods have been attempted to prepare g-C$_3$N$_4$ film. There are few reports about g-C$_3$N$_4$ grown directly on the conductive transparent glasses substrate. Raziq et al. have adopted doctor blade method to prepare the g-C$_3$N$_4$ film, the current den-

sity of the g-C$_3$N$_4$ film under visible-light irradiation ($\lambda < 600$ nm) is measured to be 0.04 mA/cm^2 at 1.0 eV (versus Ag/AgCl electrode) in 0.5 M Na$_2$SO$_4$ solution [22]. Zhang et al. have used coating method to obtain the g-C$_3$N$_4$ film (TF-CN-Sol), the obtained photocurrent density of g-C$_3$N$_4$ film (TF-CN-Sol) electrode is 8 μA/cm^2 at -0.2 V (versus Ag/AgCl electrode) [23]. However, the coating deposition method results in the uneven coverage of the g-C$_3$N$_4$ film due to the poor solubility and dispersibility of g-C$_3$N$_4$. In addition, the g-C$_3$N$_4$ film peels off easily after drying owing to the weak adhesion with substrate. Shalom et al. have used the cyanuric acid-melamine supramolecular complex (CM) to grow C$_3$N$_4$ film directly on conductive transparent glass in order to demonstrate electrochemical H$_2$ evolution reactions, but the C$_3$N$_4$ layer ($\sim$40 nm) is too thin to achieve the sufficient light absorption [24].

Herein we report a novel method, thermal vapor liquid-polymerization, which is employed to prepare the framework g-C$_3$N$_4$ film on the fluorine-doped tin oxide (FTO) glass substrate directly. The framework g-C$_3$N$_4$ film is ultimately served as photoanode for PEC water splitting to produce hydrogen for the first time. Compared with each method, this method not only owns the simple operability of thermal condensation method, but also it makes film own the better adhesion due to liquid growing on substrate. Thus the framework structure of the g-C$_3$N$_4$ film is generated by the released gas during the thermal decomposition, the adhesion of the g-C$_3$N$_4$ film with FTO surface is enhanced to depend on the liquid growth. The characterization results indicate that the framework structure of the g-C$_3$N$_4$ film is generated by the released gas during the thermal decomposition, the adhesion of the g-C$_3$N$_4$ film with FTO surface is enhanced to depend on the liquid growth. The characterization results indicate that the framework g-C$_3$N$_4$ film on FTO is complanate and uniform. It absorbs visible light with an absorption edge around 460 nm as well as corresponds to the band gap of $\sim$2.6 eV. It exhibits a better photoelectrochemical performance with the photocurrent of 89 μA/cm^2 at the bias of 1.1 V versus reversible hydrogen electrode (RHE) with 0.1 M Na$_2$SO$_4$ as the electrolyte solution. In brief, the framework g-C$_3$N$_4$ film prepared by thermal vapor liquid-polymerization possesses the following merits: (i) the uniformity of film has been demonstrated to decrease defects; (ii) the framework structure has been achieved to increase the reflections of the light so that it enhances the light harvesting ability; (iii) the smaller band gap of film has increased the light absorption so as to enhance its optical performance; (iv) photogenerated electron-hole pairs has been easily separated to improve photocurrent due to the faster charge transfer rate.

2. Experimental section

2.1. Preparation of framework g-C$_3$N$_4$ film

The framework g-C$_3$N$_4$ film is grown on FTO glass substrates directly by thermal vapor liquid-polymerization. FTO is cleaned by ultrasonication in acetone, isopropanol and ethanol for every 30 min in turn. These cleaned FTO is dried in air for 10 min. The cheap organic monomers are chosen as g-C$_3$N$_4$ precursors such as thiourea and urea. In a typical synthesis procedure, the framework g-C$_3$N$_4$ film and g-C$_3$N$_4$ bulk are synchronously obtained, as shown in Fig.S1. Firstly, the thiourea powder is obtained easily by grinding, and then 3 g of thiourea powder is transferred into a 5 ml of ceramic crucible. The ceramic crucible is totally covered by the dried FTO with the conductive surface down to it. Secondly, the crucibles are put in a muffle furnace or tube furnace and heated to 200 °C at a heating rate of 2 °C/min under air or nitrogen atmosphere for 1 h so as to undergo fully various reactions. Finally, the samples are reached to the desired temperature (500 °C or 600 °C) for 2 h so as to ensure the sample sufficiently crystallized. After naturally cool-

ing down to room temperature, the framework g-C$_3$N$_4$ film on FTO is achieved.

2.2. Characterization

The crystal structures of as-prepared g-C$_3$N$_4$ film are characterized by X-ray diffraction (XRD) using a Rigaku D/max-2500 with Cu Kα radiation ($\lambda = 0.154059$ nm). The thermal properties of thiourea are investigated in a corundum crucible under N$_2$ atmosphere by applying DTU−2 B simultaneous thermal analyzer, the controlled temperature range is from 20 °C (room temperature) to 500 °C at a heating rate of 10 °C/min. The morphology and structures of the g-C$_3$N$_4$ film on FTO are obtained by using a HITACHI S-4800I field-emission scanning electron microscope (FE-SEM) and HITACHIH-7650 transmission electron microscope (TEM) at an accelerating voltage of 100 kV. Meanwhile, the elemental mapping images of the g-C$_3$N$_4$ film are acquired by the energy dispersive spectrum (EDS) detector of FE-SEM. For TEM and high-resolution TEM (HRTEM) observations, the g-C$_3$N$_4$ film is scraped from the FTO and then dissolves in ethanol as well as drop it on a carbon coated copper grid. The UV–vis absorption spectra characterization of the g-C$_3$N$_4$ film is carried out by a DU−8 B UV–vis double-beam spectrophotometer at room temperature. The PEC performance of the g-C$_3$N$_4$ film is examined in 0.1 M Na$_2$SO$_4$ electrolyte and which is performed via an electrochemical workstation, a xenon lamp (100 mW cm^{-2}) with global AM 1.5 G is used as light source, the framework g-C$_3$N$_4$ film on FTO is used as working photoelectrode, a platinum foil as counter electrode and saturated Ag/AgCl as reference electrode. The saturated Ag/AgCl electrode in the recorded results has been converted to the reversible hydrogen electrode (RHE).

3. Results and discussion

The XRD pattern of as-prepared g-C$_3$N$_4$ film is presented in Fig. 1a. It can be obviously seen that two characteristic peaks of g-C$_3$N$_4$ exist at around 13° and 27°. Additionally, other small diffraction peaks are coincident with the FTO marked with "♦" (JCPDS Card No. 46-1088). The small characteristic peak at around 13° represents (100) facet and corresponds to the in-planar repeated period of 0.655 nm, which substantially matches with the dimensions of in-planar repeated period of tri-s-triazine unit (0.713 nm) as shown in the inset of Fig. 1a. The smaller in-planar spacing is presumably attributed to the existence of small tilt angularity in the g-C$_3$N$_4$ structure [11,25]. The strongest characteristic peak at around 27° is indexed as (002) facet, which reveals an in-planar spacing of about 0.325 nm. It is usually observed in graphitic materials because of the inter-layer stacking interaction of the conjugated aromatic system [11,25]. The two XRD peaks of as-prepared products are also consistent with the previous reported results about bulk powder g-C$_3$N$_4$. Thus the g-C$_3$N$_4$ film based on tri-s-triazine rings is directly obtained on FTO via thermal vapor liquid-polymerization method.

To support our view of a thermal vapor liquid-polymerization g-C$_3$N$_4$ film growth method, the thermal properties of thiourea are investigated. Fig. 1b displays the TG and DTA curves of thiourea. In the thermolysis process of thiourea, it can be easily seen that the thiourea almost remains unchanged until 170 °C, however, one stage of huge mass loss occurs between 170 °C and 235 °C, the weight of the sample decreases rapidly by 74%, indicating that it starts to dehydrate because thiourea is easily deliquescent when it is milled in air, as well as occurs a series of relevant transformations. The strongest endothermic peak which appears at around 180 °C should be the melting point of thiourea. At this temperature the thiourea starts to turn to liquid state. Meanwhile, maybe there
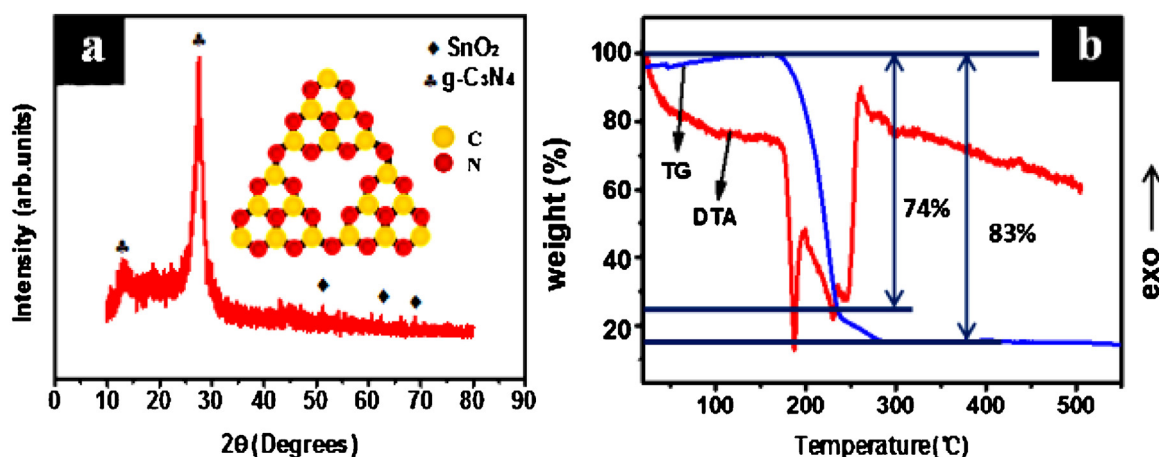
Fig. 1. (a) XRD and tri-s-triazine unit (inset) of the framework g-C_3N_4 film on FTO, (b) TG and DTA curves of the framework g-C_3N_4 film composed from thiourea in nitrogen.

occurs a relevant allotrope transformations, from some thiourea to ammonium thiocyanate, etc [26]. During this period, the following reactions could take place:

$$CN_2H_4S(s) \rightarrow CN_2H_4S(l) \tag{1}$$

$$CN_2H_4S(l) \rightarrow NH_4SCN \tag{2}$$

When the temperature is up to 236 °C, it can be seen that there is a small endothermic peak which indicates the transformation of thiourea into cyanamide. Cyanamide is commonly used to synthesize g-C_3N_4. At this time, a number of gas (for example, NH_3) will be produced, corresponding to the reaction equation is:

$$2CN_2H_4S \rightarrow CH_2N_2 + CS_2 + 2NH_3 \tag{3}$$
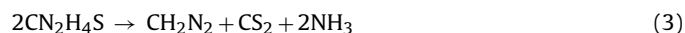
According to the reaction equation, the weight loss is accurately calculated to 72.4% which is nearly consistent with the actual weight loss of 74%. The actual weight loss is a little bigger than the calculated one which may be caused by the volatilization of impurity in the raw material. With the further increasing temperature, the continuous weight loss is about 9% in the temperature during 235–300 °C, the weak peak at 255 °C implies that it corresponds well to the reaction from cyanamide to melamine:

$$3CH_2N_2 \rightarrow C_3H_6N_6 \tag{4}$$

With further heating, the sample continues to the further condensation process, resulting in the final product g-C_3N_4, which mainly depends on the following reaction equation:

$$C_3H_6N_6 \rightarrow g\text{-}C_3N_4 + 2NH_3 \tag{5}$$

In addition, a series of thermolysis condensation reactions above are briefly shown in Fig. 2.

To confirm the morphology detail of the g-C_3N_4 film on FTO, morphology detail has been researched. SEM images of typical top view as well as the enlarged-view of the g-C_3N_4 film are shown in Fig. 3a and b. Fig. 3a shows that the g-C_3N_4 film possesses a number of irregular porous that interconnect together to form framework structure, which could be the consequence of the released gas (H_2O, NH_3, etc.) during the thermal decomposition of thiourea [27]. Moreover, the different kinds of gas are released when thiourea is decomposed. The different release speed rates and stress could result in the irregular shape of the pores which connect with each other into framework structure finally. It deserves to be mentioned that porous framework structure could effectively increase the surface area because the area of camber is larger than that of plane in the same space, which will be beneficial to improve the PEC ability by providing lots of reactive sites. In addition, some layered surface morphology structures are also found such as the selected

region marked by the red lines in Fig. 3a, which is in agreement with the graphite-like carbon nitride by typical structural characteristic [21]. Fig. 3b displays that the size of porous is different. The diameter of the porous on the film surface is approximately 0.7–8 μm. The molecular mass of varied release gas is different (for instance, molecular mass of NH_3 is 17), which contributes to the different sizes of pores. Distinctively, the framework surface of g-C_3N_4 film is smooth by virtues of the liquefied growth. On the one hand, thermal vapor may become ultra-small droplets once contacted with the FTO and grow directly. On the other hand, thermal vapor perhaps carries with ultra-small droplets together to reach the FTO. The thermal vapor starts to crystallize with the ultra-small droplets as crystal nuclei and grow, this model of crystal growth can reduce the energy needed for crystal growth. In addition, the liquefied growth of film can enhance the adhesion of the g-C_3N_4 film with FTO surface. Meanwhile, the elemental mapping images of the g-C_3N_4 film are obtained, and its selected area is marked by the red lines in Fig. 3b. It verifies that C and N elements uniformly distribute in the g-C_3N_4 film, as well as Sn and O elements come from FTO. From the SEM image shown in Fig. 3c, it can be clearly seen that the framework g-C_3N_4 film has been successfully grown on FTO. The thickness of the framework g-C_3N_4 film ranges ~2 μm, which is considerably complanate and uniform. However, the uniformity of the film relies mainly on the preparation method. Raw materials rise in the form of thermal vapor which has a good dispersibility. Thus, the same amount material vapor arrives at the every corner of the FTO at the same time, which makes the consistent thickness substantially to promote uniformity of the film.

The morphology and structures of the g-C_3N_4 film are further investigated. The HRTEM in Fig. 4a shows that the g-C_3N_4 film exhibits clearly thin and irregular multilayer structure, corresponded to the typical structural features of graphite-like carbon nitride again. It can be found that about four or five layers exist from the edge to the inner of the sample. The TEM in Fig. 4b reveals that the g-C_3N_4 film has porous structure with the diameter of ~100 nm which is not in agreement with the SEM image in Fig. 3b. It may be aroused by the porous structure shown in the TEM is the internal morphology of the g-C_3N_4 film while the porous structure shown in the SEM image is the external morphology of the g-C_3N_4 film. In addition, it can be also seen that holes exist in the inner of g-C_3N_4 film from Fig. 3c. The crystal growth rate is more quickly than the discharge velocity of the gas so that gas becomes bubbles retained inside during the heating process. The inset of Fig4b displays that the in-planar spacing value of the g-C_3N_4 film is calculated as 0.325 nm corresponding to the lattice spacing distance of (002) facet of g-C_3N_4.
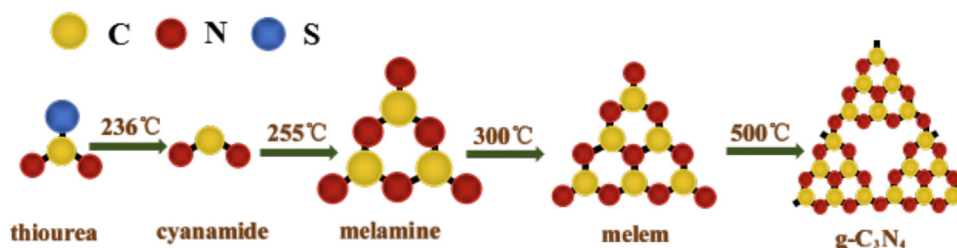
Fig. 2. TG analysis and related processes during the polycondensation of thiourea in nitrogen.
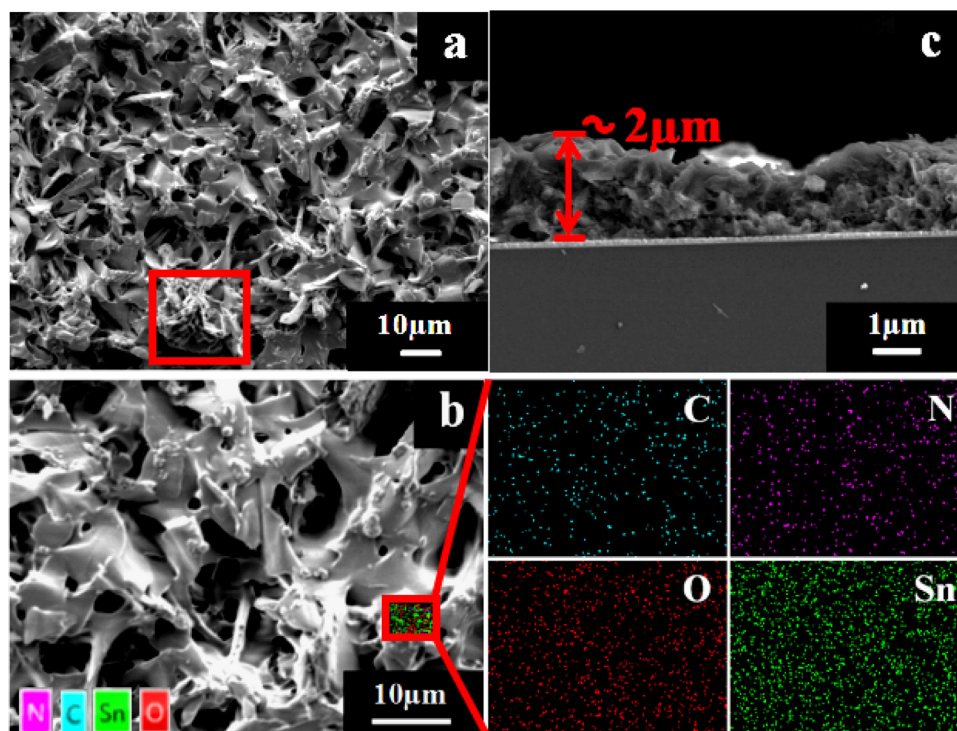

Fig. 3. Typical top view SEM image (a) and enlarged-view image with the corresponding selected area high-resolution element distribution mappings (b) and the cross-sectional view SEM image (c) of the framework g-C$_3$N$_4$ film.
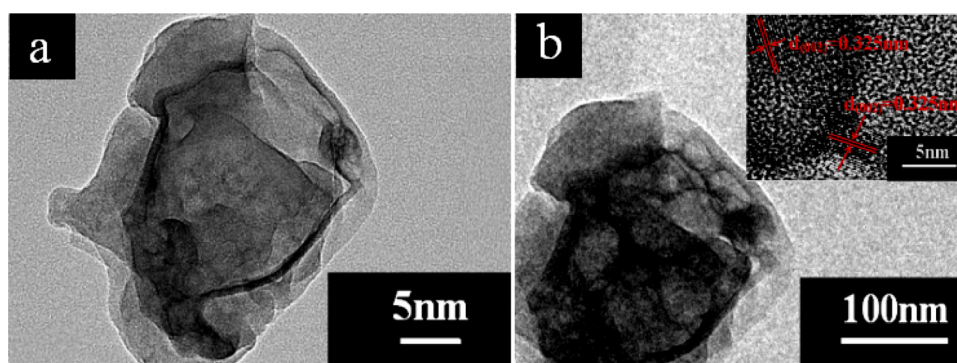

Fig. 4. TEM images (a) and (b), HRTEM image (inset of b) of the framework g-C$_3$N$_4$ film.

To elucidate the optical properties of the framework g-C$_3$N$_4$ film, the UV–vis absorption spectra characterization is carried out, the date is recorded in the wavelength range of 300–900 nm using the FTO as the reference, which is shown in Fig. 5. The framework g-C$_3$N$_4$ film shows an absorption edge of ~460 nm, which is better than the results of the former papers on g-C$_3$N$_4$ powder that are prepared through thermal condensation in air [3]. This should

be due to that the framework structure takes full advantage of the multiple reflections to enhance light harvesting ability. Every beam of light is generally reflected on the surface of the g-C$_3$N$_4$ film once at most. However, as shown in Fig.S2, when light is irradiated in the inner of the framework structure, it could be reflected much more times in irregular porous and interconnect layers. Thus, the
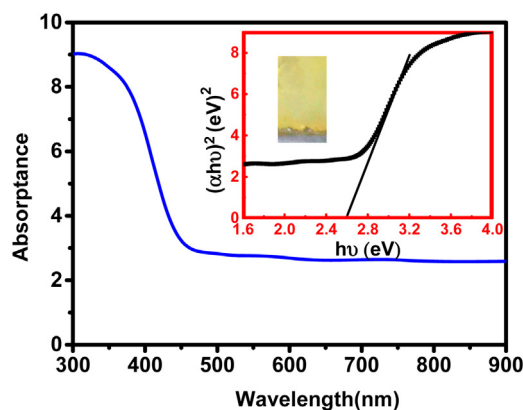
Fig. 5. Ultraviolet-visible diffuse reflectance spectrum and plot of $(\alpha h\upsilon)^2$ versus $h\upsilon$ (inset) of the framework g-C_3N_4 film.
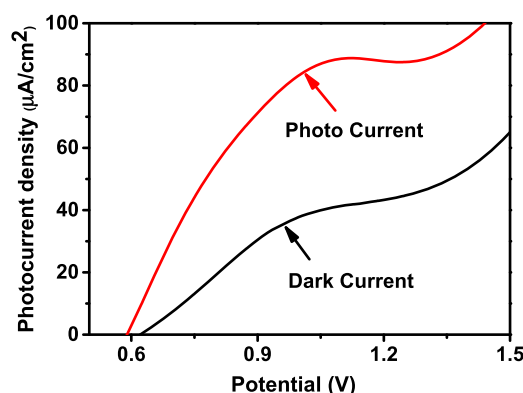

Fig. 6. Photo and dark current density-potential curves of the framework g-C_3N_4 film.

Fig. 7. Linear sweep voltammograms of the framework g-C_3N_4 film.

multiple reflections take place in framework structure to promote light utilization and harvesting.

Subsequently, the band gap (Eg) of the framework g-C_3N_4 film is confirmed by the following equation [28]:

$$(\alpha h\upsilon)^n = A(h\upsilon - Eg) \tag{6}$$

Where α represents the absorbance coeffcient, h is the Planck constant, υ is the light frequency and A is a constant, respectively. Based on the type of the semiconductor, when n is 2 for the direct band gap and 1/2 for an indirect band gap. According to Eq. (6), and g-C_3N_4 is direct band gap semiconductor [29], the band gap of the framework g-C_3N_4 film is calculated by 2.6 eV approximately, which shows in the inset of Fig. 5. Additionally, the framework g-C_3N_4 film is quite uniform, its surface is more complanate and fewer defects such as some raised blocks (as shown in the inset macrographic photograph of Fig. 5). It can be noted that the band gap value is suitable for visible light absorption and improves the optical performance of the film. Finally, the higher visible absorption of the film should be due to not only that the framework structure enhances light harvesting ability, but also that its smaller band gap improves its optical performance.

To investigate the PEC properties of the framework g-C_3N_4 film, the linear sweep voltammogram (LSV) in the potential ranging from 0.5 to 1.50 V vs RHE is measured in 0.1 M Na_2SO_4 aqueous solution. What can be shown evidently in Fig. 6 is that the dark current density of the framework g-C_3N_4 film is 40 µA/cm² at 1.1 V (vs. RHE). However, the photocurrent density is 89 µA/cm² at 1.1 V (vs. RHE). This photocurrent density of the framework g-C_3N_4 film is higher than that of the g-C_3N_4 film derived by a doctor blade method [22]. and by g-C_3N_4 sol coating method [23]

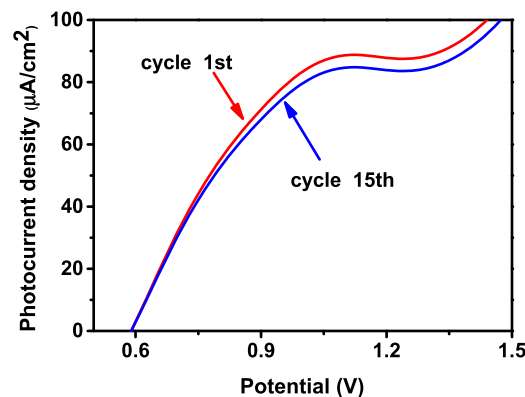from g-C_3N_4 powder, respectively. In order to further measure the performance of the framework g-C_3N_4 film, the electrochemical impedance spectroscopy (EIS) is obtained by using the same electrochemical workstation in Fig.S3. Fig.S3 shows that the EIS Nyquist plot of the framework g-C_3N_4 film consists of two semicircles. The equivalent circuit is displayed as the inset of Fig.S3, in which Rs is serial resistance, R_1 and C_1 are the bulk charge transfer resistance and capacity of the samples, R_2 and C_2 are the charge transfer resistance and capacity from the samples surface to electrolyte. Definitely, reduced the recombination of photogenerated electron-hole pairs leads to a higher concentration of charge carriers, which shows a smaller arc radius. However, when lots of photogenerated electrons arrive at the interface of the sample and electrolyte, it would cause the recombination of photogenerated electron-hole pairs, which displays a bigger arc radius. Based on the above mechanism, it can be seen that the framework g-C_3N_4 film presents the smaller arc radius, which would mean that it has the smaller bulk charge transfer resistance and its photogenerated electron-hole pairs are easily separated. In order to improve the charge transfer rate from the framework g-C_3N_4 film surface to electrolyte, a FeOOH co-catalyst layer is loaded using an electrochemical deposition method on the framework g-C_3N_4 film by applying a bias of 1.2 V (versus Ag/AgCl electrode) in a 0.1 M $FeCl_2$ solution for about 5 min [30]. Their photocurrent density and EIS are shown in Fig.S4a and Fig.S4b, respectively. The photocurrent density of the g-C_3N_4/FeOOH is approximately 122 µA/cm² at 1.1 V (vs. RHE), and the g-C_3N_4/FeOOH displays a smaller arc radius than that of the framework g-C_3N_4 film. FeOOH, as co-catalyst [31,32], enhances the photogenerated electron-hole pairs separation and transfer rate of the framework g-C_3N_4 film. Therefore, it can be known that the photogenerated electron-hole pairs of the framework g-C_3N_4 film are easily separated and transferred. Further studies are under investigation to improve the photogenerated electron-hole pairs separation and transfer rate of the g-C_3N_4 film by choosing other co-catalysts. In a word, the excellent photocurrent density of the framework g-C_3N_4 film is owing to the following causes: (i) the film is uniform with few defects; (ii) its light harvesting ability is enhanced thanks to its framework structure; (iii) its optical performance is improved due to smaller band gap; (iv) photogenerated electron-hole pairs recombination is reduced because of the faster charge transfer rate.

Furthermore, to survey the stability of the framework g-C_3N_4 film, linear sweep voltammogram is measured from 1 to 15 cycles under illumination, the results are recorded in Fig. 7. The 15th photocurrent density of the framework g-C_3N_4 film is 95.5% of the 1 st photocurrent density with the value of 85 µA/cm² at 1.1 V (Vs RHE). It can be seen that the framework g-C_3N_4 film presents certain stability. Specially, it can be found that the photocurrent density of the framework g-C_3N_4 film is relatively stable in the early test,

but with the time goes by, the 60th photocurrent density of the framework g-C_3N_4 film declines sharply to 37 $\mu A/cm^2$ at 1.1 V (Vs RHE) (as shown in Fig.S5). The framework g-C_3N_4 film is dried after photocurrent density test, and then its microcosmic morphology is analyzed using SEM and its macrographic photo is displayed to compare with the initial g-C_3N_4 film (as shown in the inset of Fig.S5). It can be noted that the film is not entire after photocurrent density test which may be the reason of declined photocurrent density. The film starts to peel from the FTO due to the added bias potential and immersed in electrolyte solution for a long time. Further studies are under investigation to improve the adhesion of the framework g-C_3N_4 film such as changing the thickness of film, which will be published in elsewhere.

4. Conclusions

In summary, we have prepared a novel framework structure g-C_3N_4 film by a thermal vapor liquid-polymerization method for PEC water splitting. The framework g-C_3N_4 film shows improved PEC performance with photocurrent density of 89 $\mu A/cm^2$ at 1.1 V (vs. RHE). It should be found that the outstanding PCE performance of the framework film is due to the uniform surface, increased light harvesting ability, improved optical performance and reduced photogenerated electron-hole pairs recombination. We hope that our reports could provide a new insight into the fabrication of g-C_3N_4 film with framework structure by thermal vapor liquid-polymerization method which applied in PEC water splitting to produce H_2.

Acknowledgments

Appendix A. Supplementary data

Supplementary data associated with this article can be found, in the online version, at http://dx.doi.org/10.1016/j.apcatb.2017.03.030.

References

[1] C. Marchal, M. Behr, F. Vigneron, V. Caps, V. Keller, Au/TiO_2 photocatalysts prepared by solid grinding for artificial solar-light water splitting, New J. Chem. 40 (2016) 4428–4435.

[2] A. Fujishima, K. Honda, Electrochemical photolysis of water at a semiconductor electrode, Nature 238 (1972) 37–38.

[3] Q. Tay, P. Kanhere, C.F. Ng, S. Chen, S. Chakraborty, A.C.H. Huan, T.C. Sum, R. Ahuja, Z. Chen, Defect engineered g-C_3N_4 for efficient visible light photocatalytic hydrogen production, Chem. Mater. 27 (2015) 4930–4933.

[4] K.Y. Guo, Z.F. Liu, Y. Wang, Y.F. Zhao, Y.C. Xiao, J.H. Han, Y.J. Li, B. Wang, T. Cui, Fabrication of ZnO/$SrTiO_3$ nanoarrays and its photoelectrochemical performances, Int. J. Hydrogen Energy 39 (2014) 13408–13414.

[5] S.Q. Peng, M. Ding, T. Yi, Y.X. Li, Photocatalytic hydrogen evolution in the presence of pollutant methylamines over Pt/$ZnIn_2S_4$ under visible light irradiation, J. Mol. Catal. 28 (2014) 466–473.

[6] J.H. Han, Z.F. Liu, K.Y. Guo, X.Q. Guo, Bo Wang, X.Q. Zhang, T.T. Hong, High-efficiency photoelectrochemical electrodes based on $ZnIn_2S_4$ sensitized ZnO nanotube arrays, Appl. Catal. B: Environ. 163 (2015) 179–188.

[7] G.J. Liu, J.Y. Shi, F.X. Zhang, Z. Chen, J.F. Han, C.M. Ding, S.S. Chen, Z.L. Wang, H.X. Han, C. Li, A tantalum nitride photoanode modified with a hole-storage layer for highly stable solar water splitting, Angew. Chem. Int. Ed. 53 (2014) 7295–7299.

[8] C.Y. Liu, H.W. Huang, X. Du, T.R. Zhang, N. Tian, Y.X. Guo, Y.H. Zhang, In situ co-crystallization for fabrication of g-C_3N_4/Bi_5O_7I heterojunction for enhanced visible-light photocatalysis, J. Phys. Chem. C 119 (2015) 17156–17165.

[9] J.D. Hong, X.Y. Xia, Y.S. Wang, R. Xu, Mesoporous carbon nitride with in situ sulfur doping for enhanced photocatalytic hydrogen evolution from water under visible light, J. Mater. Chem. 22 (2012) 15006–15012.

[10] X.Q. Fan, L.X. Zhang, R.L. Cheng, M. Wang, M.L. Li, Y.J. Zhou, J.L. Shi, Construction of graphitic C_3N_4-based intramolecular donor–acceptor conjugated copolymers for photocatalytic hydrogen evolution, ACS Catal. 5 (2015) 5008–5015.

[11] X.C. Wang, K. Maeda, A. Thomas, K. Takanabe, G. Xin, J.M. Carlsson, K. Domen, M. Antonietti, A metal-free polymeric photocatalyst for hydrogen production from water under visible light, Nat. Mater. 8 (2009) 76–82.

[12] W.H. Brito, J. da Silva-Araújo, H. Chacham, G-C_3N_4 and others: predicting new nanoporous carbon nitride planar structures with distinct electronic properties, J. Phys. Chem. C 119 (2015) 19743–19751.

[13] J.J. Liu, Origin of high photocatalytic efficiency in monolayer g-C_3N_4/CdS heterostructure: a hybrid DFT study, J. Phys. Chem. C 119 (2015) 28417–28423.

[14] F. Dong, Z.Y. Wang, Y.H. Li, W.K. Ho, S.C. Lee, Immobilization of polymeric g-C_3N_4 on structured ceramic foam for efficient visible light photocatalytic air purification with real indoor illumination, Environ. Sci. Technol. 48 (2014) 10345–10353.

[15] F. Dong, Z.W. Zhao, Y.J. Sun, Y.X. Zhang, S. Yan, Z.B. Wu, An advanced semimetal-organic bi spheres-g-C_3N_4 nanohybrid with SPR-enhanced visible-light photocatalytic performance for NO purification, Environ. Scie. Technol. 49 (2015) 12432–12440.

[16] S.W. Zhang, J.X. Li, X.K. Wang, Y.S. Huang, M.Y. Zeng, J.Z. Xu, In situ ion exchange synthesis of strongly coupled Ag@ AgCl/g-C_3N_4 porous nanosheets as plasmonic photocatalyst for highly efficient visible-light photocatalysis, ACS Appl. Mater. Interfaces 6 (2014) 22116–22125.

[17] X.Q. Fan, Z. Xing, Z. Shu, L.X. Zhang, L.Z. Wang, J.L. Shi, Improved photocatalytic activity of g-C_3N_4 derived from cyanamide-urea solution, RSC Adv. 5 (2015) 8323–8328.

[18] J.K. Gao, J.P. Wang, X.F. Qian, Y.Y. Dong, H. Xu, R.J. Song, C.F. Yan, H.C. Zhu, Q.W. Zhong, G.D. Qian, J.M. Yao, One-pot synthesis of copper-doped graphitic carbon nitride nanosheet by heating Cu-melamine supramolecular network and its enhanced visible-light-driven photocatalysis, J. Solid State Chem. 228 (2015) 60–64.

[19] J. Wan, S.Z. Hu, F.Y. Li, Z.P. Fan, G. Lu, J. Zhang, Preparation of mesoporous carbon nitride photocatalyst with tunable band structure by copolycondensation of dicyandiamide and urea, Asian J. Chem. 26 (2014) 8553–8556.

[20] J.S. Zhang, M.W. Zhang, R.Q. Sun, X.C. Wang, A facile band alignment of polymeric carbon nitride semiconductors to construct isotype heterojunctions, Angew.e Chem. 124 (2012) 10292–10296.

[21] D.L. Jiang, J. Li, C.S. Xing, Z.Y. Zhang, S.C. Meng, M. Chen, Two-dimensional $CaIn_2S_4$/g-C_3N_4 heterojunction nanocomposite with enhanced visible-light photocatalytic activities: interfacial engineering and mechanism insight, ACS Appl. Mater. Interfaces 7 (2015) 19234–19242.

[22] F. Raziq, Y. Qu, X.L. Zhang, M. Humayun, J. Wu, A. Zada, H.T. Yu, X.J. Sun, L.Q. Jing, Enhanced cocatalyst-free visible-light activities for photocatalytic fuel production of g-C_3N_4 by trapping holes and transferring electrons, J. Phys. Chem. C 120 (2015) 98–107.

[23] J.S. Zhang, M.W. Zhang, L.H. Lin, X.C. Wang, Sol processing of conjugated carbon nitride powders for thin-film fabrication, Angew. Chem. Int. Ed. 54 (2015) 6297–6301.

[24] M. Shalom, S. Gimenez, F. Schipper, F. Schipper, I. Herraiz-Cardona, J. Bisquert, M. Antonietti, Controlled carbon nitride growth on surfaces for hydrogen evolution electrodes, Angewandte Chemie 126 (2014) 3728–3732.

[25] S. Yang, X. Feng, X.C. Wang, K. Mullen, Graphene-based carbon nitride nanosheets as efficient metal-free electrocatalysts for oxygen reduction reactions, Angew. Chem. Int. Ed. 50 (2011) 5339–5343.

[26] W. Ji, S. Jing, J.L. Liu, D.M. Zhang, B. Yu, Synthesis and application of thisourea, Chem. Ind. Times 18 (2004) 10–15.

[27] B. Hu, F.P. Cai, T.J. Chen, M.S. Fan, C.J. Song, X. Yan, W.D. Shi, Hydrothermal synthesis g-C_3N_4/Nano-$InVO_4$ nanocomposites and enhanced photocatalytic activity for hydrogen production under visible light irradiation, ACS Appl. Mater. Interfaces 7 (2015) 18247–18256.

[28] J. Zhang, Z.H. Liu, Z.F. Liu, Novel WO_3/Sb_2S_3 heterojunction photocatalyst based on WO_3 of different morphologies for enhanced efficiency in photoelectrochemical water splitting, ACS Appl. Mater. Interfaces 8 (2016) 9684–9691.

[29] L. Ge, C.C. Han, J. Liu, Y.F. Li, Enhanced visible light photocatalytic activity of novel polymeric g-C_3N_4 loaded with Ag nanoparticles, Appl. Catal. A: Gen. 409 (2011) 215–222.

[30] C.R. Lhermitte, J.G. Verwer, B.M. Bartlett, Improving the stability and selectivity for the oxygen-evolution reaction on semiconducting WO_3 photoelectrodes with a solid-state FeOOH catalyst, J. Mater. Chem. A 4 (2016) 2960–2968.

[31] C.M. Ding, J.Y. Shi, Z.L. Wang, C. Li, Photoelectrocatalytic water splitting: significance of cocatalysts, Electrolyte and Interfaces, ACS Catal. 7 (2017) 675–688.

[32] T.W. Kim, K.S. Choi, Nanoporous $BiVO_4$ photoanodes with dual-layer oxygen evolution catalysts for solar water splitting, Science 343 (2014) 990–994.